

Production of sodium Bose–Einstein condensates in an optical dimple trap

This article has been downloaded from IOPscience. Please scroll down to see the full text article.

2011 New J. Phys. 13 065022

(<http://iopscience.iop.org/1367-2630/13/6/065022>)

View [the table of contents for this issue](#), or go to the [journal homepage](#) for more

Download details:

IP Address: 129.199.119.233

The article was downloaded on 28/10/2011 at 09:59

Please note that [terms and conditions apply](#).

Production of sodium Bose–Einstein condensates in an optical dimple trap

D Jacob^{1,3}, E Mimoun¹, L De Sarlo¹, M Weitz², J Dalibard¹
and F Gerbier¹

¹ Laboratoire Kastler Brossel, ENS, UPMC-Paris 6, CNRS, 24 rue Lhomond, 75005 Paris, France

² Institut für Angewandte Physik, Universität Bonn, Wegelerstr. 8, 53115 Bonn, Germany

E-mail: david.jacob@lkb.ens.fr

New Journal of Physics **13** (2011) 065022 (16pp)

Received 1 April 2011

Published 28 June 2011

Online at <http://www.njp.org/>

doi:10.1088/1367-2630/13/6/065022

Abstract. We report on the realization of a sodium Bose–Einstein condensate (BEC) in a combined red-detuned optical dipole trap formed by two beams crossing in a horizontal plane and a third, tightly focused dimple trap (dT) propagating vertically. We produce a BEC in three main steps: loading of the crossed dipole trap from laser-cooled atoms, an intermediate evaporative cooling stage that results in efficient loading of the auxiliary dT, and a final evaporative cooling stage in the dT. Our protocol is implemented in a compact setup and allows us to reach quantum degeneracy even with relatively modest initial atom numbers and available laser power.

³ Author to whom any correspondence should be addressed.

Contents

1. Introduction	2
2. Experimental setup	3
2.1. Laser cooling	3
2.2. Trapping laser configuration	4
2.3. Imaging	5
3. Loading and free evaporation in the crossed dipole trap (CDT)	6
3.1. Dipole trap loading dynamics	6
3.2. Optimization of CDT loading	7
4. Two-stage evaporation	10
4.1. Evaporation in the CDT alone	10
4.2. Evaporation in the dimple trap	10
5. Conclusion and prospects	12
Acknowledgments	13
Appendix A. Analysis of CDT images	13
References	15

1. Introduction

The preparation of degenerate atomic quantum gases is interesting from both a fundamental and an applied point of view. On the one hand, the unprecedented level of control on these systems allows one to study quantum many-body phenomena in the absence of perturbing effects unavoidable in solid-state systems [1]. On the other hand, degenerate gases are a promising starting point to reliably produce highly entangled states, which could pave the way for a new generation of atom-based quantum sensors (see [2, 3] and references therein).

In view of the sensitivity of these strongly correlated states to the perturbations caused by magnetic field fluctuations, experimental schemes in which evaporative cooling is performed without the use of external magnetic fields are particularly interesting. These so-called ‘all-optical evaporation’ schemes rely on far off-resonant optical dipole traps. They have been developed by several groups to produce Bose–Einstein condensates (BECs) of various atomic species, in particular alkali atoms (Rb [4–6], Li [7], Cs [8] and Na [9]). In such all-optical setups, the trapping potential is almost independent of the internal state, opening the route to the study of spinor condensates [10].

Experiments relying on all-optical setups are based on a common experimental scheme: laser-cooled atoms are first loaded into an optical dipole trap and then evaporatively cooled by lowering the trapping laser intensity and thus the trap depth. In this paper, we discuss how to optimize these two steps for producing an all-optical BEC of sodium atoms, starting with relatively modest atom numbers and laser powers.

The first issue, dealing with the transfer from the magneto-optical trap (MOT) to the optical dipole trap, has extensively been studied (see e.g. [11]). Laser cooling forces and light-assisted losses can be strongly modified by the presence of the dipole trap potential. The size and depth of the trapping potential have to be adapted to the size, density and temperature of the MOT. A convenient configuration is a laser trap consisting of two crossed Gaussian beams [12], as

in our experiment. The loading of the trap then occurs in two steps: atoms are first captured in both arms of the trap and then start filling the crossing region by ‘free evaporation’ once the near-resonant cooling beams have been turned off [4]. We will describe our procedure to optimize the atom number N in the crossing region and the temperature T at the end of the free evaporation to obtain a high phase-space density \mathcal{D} and a large collision rate γ_{coll} . We recall that $\mathcal{D} = N(\hbar\omega/k_{\text{B}}T)^3$ and $\gamma_{\text{coll}} \propto N/\omega^3T$ for a Boltzmann gas in a harmonic trap, with \hbar being the Planck constant, k_{B} the Boltzmann constant and ω the average trapping frequency. For a given beam size, we find that the optimal trap depths for loading and free evaporation differ. We suggest that trap-induced light shifts on the cooling transition is the physical mechanism underlying this observation.

The second issue is related to the efficiency of evaporative cooling. In this respect, optical traps differ in several aspects from magnetic traps. In magnetic traps, evaporative cooling takes place in the so-called runaway regime, where the elastic collision rate γ_{coll} and evaporation efficiency stay constant or even increase with time [13]. In optical traps, this regime is not easily reachable because the trap depth and trap confinement both increase with the trapping laser power. In practice, decreasing the trap depth to force evaporation results in a looser confinement, so that the collision rate can decrease even if the phase-space density increases. Solutions involving modification of the trapping potential have been demonstrated to resolve this issue. For example, a dynamical change in the beam size using a zoom lens allows one to maintain constant confinement while reducing the trap depth [5], thus preserving a high collision rate during evaporation. Runaway evaporation in an optical trap can also be obtained by using an additional expelling potential independent of the trapping laser (gravity or ‘pulling’ laser) in order to decouple trap confinement and potential depth [14, 15]. A third solution, based on the addition of a tighter ‘dimple’ potential [8, 16], has been realized and characterized theoretically [17–19]. This solution, which is the one investigated in this paper, leads to a two-step evaporation sequence: after the loading of a larger trap, atoms are first transferred by cooling into the ‘dimple’ trap (dT) and then further cooled down in this trap. The major advantages of this technique are its relative technical simplicity (as compared, for instance, with a ‘zoom-lens’ method), the increase in phase-space density during the transfer and the high efficiency of the second evaporation step due to the high confinement in the ‘dT’. Here we describe the first application of this technique to ^{23}Na . Starting with 3×10^5 trapped atoms, a BEC of $\sim 10^4$ ^{23}Na atoms is produced after ~ 2 s evaporation time.

This paper is organized as follows. In section 2, we give an overview of our experimental setup. In section 3, we investigate the loading of a dipole trap from a MOT of sodium atoms and study how the compression of the trap after the atom capture improves the initial conditions for evaporative cooling. We then present, in section 4, how evaporative cooling works in the presence of the auxiliary dT, detailing its filling dynamics, and the last evaporative cooling stage to reach Bose–Einstein condensation.

2. Experimental setup

2.1. Laser cooling

Our experiment starts with a sodium MOT capturing approximately 10^7 atoms in 10 s from a vapor whose pressure is modulated using light-induced atomic desorption [20]. After the MOT is formed, a far off-resonant dipole trap is switched on (see section 2.2). The detunings and

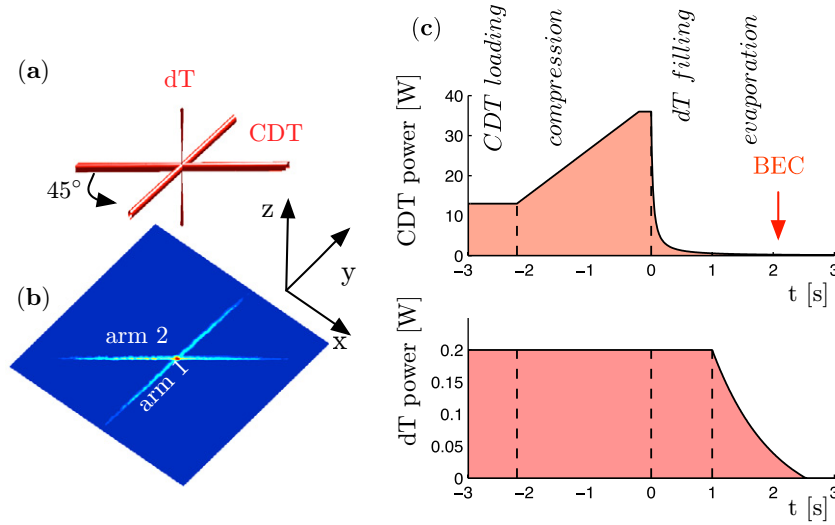


Figure 1. (a) Sketch of the laser geometry showing the CDT propagating in the horizontal plane and the dT propagating vertically. (b) Fluorescence image of atoms trapped in the CDT, taken after a short time-of-flight. The thermal equilibrium state in such a potential has a characteristic spatial structure: two elongated ‘arms’ and a denser crossing region. (c) Evolution of the powers of the CDT and the dT during the sequence. The first step corresponds to the loading of the CDT from a ‘cold-MOT’ phase, followed by a compression that helps to fill the central trapping region. The next step consists in evaporatively cooling the CDT and results in the filling of the dT. The last step is evaporative cooling in the dT, which leads to Bose–Einstein condensation.

powers of both the cooling (tuned to $3S_{1/2}$, $F = 2 \rightarrow 3P_{3/2}$, $F' = 3$ transition) and repumping (tuned to the $3S_{1/2}$, $F = 1 \rightarrow 3P_{3/2}$, $F' = 2$ transition) lasers are modified in order to optimize the trap loading. During a first ‘dark MOT’ phase [21], we lower the power of the repumping laser in about 100 ms, from $I_{\text{rep}} = 300$ to $10 \mu\text{W cm}^{-2}$ per beam while keeping the magnetic gradient on. This reduces the loss rate due to light-induced collisions by limiting the population of excited states [11]. We keep the cooling laser intensity at the same value as that for MOT loading, $I_{\text{cool}} = 0.9 \text{ mW cm}^{-2}$ per beam, which corresponds to one sixth of the saturation intensity ($I_{\text{sat}} = 6.3 \text{ mW cm}^{-2}$). During this ‘dark MOT’ phase, both the spatial density in the dipole trap and the temperature increase. We then apply a 30 ms-long ‘cold MOT’ phase, where the cooling beam detuning is shifted from $\delta_{\text{cool}} \approx -\Gamma$ to $\delta_{\text{cool}} \approx -3.8\Gamma$ ($\Gamma/2\pi \approx 10 \text{ MHz}$ is the natural linewidth). The temperature of the atoms after this cooling sequence is around $50 \mu\text{K}$.

2.2. Trapping laser configuration

The far off-resonant dipole trap results from the combination of three beams, two forming a crossed dipole trap (CDT) in the horizontal x – y plane and a tightly focused one propagating vertically along the z -axis (see figure 1(a)), which we refer to as the dT. The CDT is derived from a 40 W fiber laser (IPG Photonics) at 1070 nm. This trap is formed by folding the beam onto itself at an angle $\theta \simeq 45^\circ$ in the horizontal plane. At the crossing point, both arms have a waist $w_{\text{CDT}} \approx 42 \mu\text{m}$. We control the laser power using a motorized rotating waveplate (OWIS

Table 1. Trapping frequencies and trap depths at $P_{\text{CDT}} \approx 36 \text{ W}$ and $P_{\text{dT}} \approx 200 \text{ mW}$ for the CDT and dT, respectively.

Dipole trap	$\omega^x/2\pi$ (kHz)	$\omega^y/2\pi$ (kHz)	$\omega^z/2\pi$ (kHz)	V_0/k_B (mK)
CDT	2.5	4.5	5.1	1.2
dT	3.7	3.7	0.021	0.10

GmbH), followed by a Glan–Taylor polarizer (bandwidth $\sim 10 \text{ Hz}$) and a control input on the current in the laser pump diodes (bandwidth $\sim 50 \text{ kHz}$). The waveplate is used for the coarse reduction of laser power by changing the amount of light transmitted by the polarizer, whereas the current control is used at the end of the evaporation ramp (low laser powers) and for fast servo-control of the intensity to reduce fluctuations. Combining both servo loops, we can control the laser power from its maximal value ($P_{\text{CDT}} \approx 36 \text{ W}$) down to $\approx 100 \text{ mW}$. We can switch off the trapping potential to an extinction level greater than 90% in less than $10 \mu\text{s}$ using the laser current input. We use motorized mirrors (Agilis, Newport Corporation) for alignment. Special care is taken to ensure the orthogonality of the polarization of both arms, realized by the insertion of a $\lambda/2$ waveplate that is positioned with a precision $\lesssim 0.5^\circ$. A misalignment of only 1° results in measurable heating of the sample [20].

The auxiliary dT is produced using a 500 mW laser (Mephisto-S, InnoLight GmbH) at 1064 nm. As sketched in figure 1(a), the beam propagates vertically and crosses the CDT with a waist of $w_{\text{dT}} \approx 8 \mu\text{m}$. The laser beam is transmitted through a single-mode optical fiber and focused to a waist size w_{dT} using a custom-made microscope objective (CVI Melles Griot, $\text{NA} \gtrsim 0.3$). An acousto-optic modulator placed before the fiber allows us to control the intensity and to quickly switch off the dT beam.

To fix the notation that will be used in the following, we give here the expressions for the dipole trap potentials. The expression for the CDT potential is given by

$$V_{\text{CDT}}(x, y, z) = -\frac{V_{\text{CDT}}^0}{2} \left[\frac{e^{-2(x^2+z^2)/w(y)^2}}{(w(y)/w_{\text{CDT}})^2} + \frac{e^{-2(u^2+z^2)/w(v)^2}}{(w(v)/w_{\text{CDT}})^2} \right], \quad (1)$$

with $w(y) = w_{\text{CDT}} \sqrt{1 + y^2/y_R^2}$ and with y_R the Rayleigh length being $y_R = \pi w_{\text{CDT}}^2/\lambda \approx 5.2 \text{ mm}$. We have also introduced the rotated coordinates: $(u, v) = (x \cos(\theta) + y \sin(\theta), -x \sin(\theta) + y \cos(\theta))$. The expression for the dT potential is given by

$$V_{\text{dT}}(x, y, z) = -V_{\text{dT}}^0 e^{-2(x^2+y^2)/w_{\text{dT}}^2}, \quad (2)$$

neglecting the confinement of the dT along the z -axis, always negligible compared with the vertical confinement of the CDT. Typical trapping frequencies and potential depths are given in table 1.

In figure 1(c) is schematically presented the temporal evolution of the powers of the two lasers during the experimental sequence. This time evolution is optimized for loading and evaporation, as explained in sections 3 and 4.

2.3. Imaging

We monitor the time evolution of the trapped cloud using both fluorescence imaging and absorption imaging [22]. Fluorescence light is captured by the same high-numerical-aperture

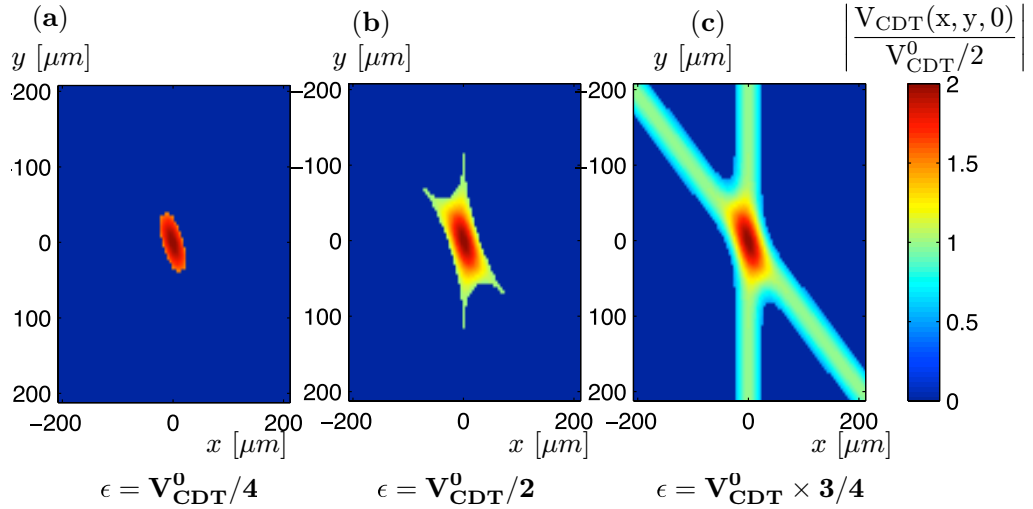


Figure 2. CDT potential in the $z = 0$ plane, truncated at an energy $\epsilon = V_{\text{CDT}}^0/4$ (a), $\epsilon = V_{\text{CDT}}^0/2$ (b) and $\epsilon = V_{\text{CDT}}^0 \times 3/4$ (c).

microscope used to focus the dT. The photons are collected on a low-noise charge-coupled device camera (PIXIS, Princeton Instruments). In figure 1(b), we show a typical fluorescence image. We typically observe the atoms after a time-of-flight of $t_{\text{ToF}} = 0.1$ ms during a short pulse ($t_{\text{mol}} = 50 \mu\text{s}$) performed with the six cooling and repumping beams.

Absorption images are recorded with a vertically propagating resonant probe beam, which is well suited for the analysis of the central denser part of the trapped cloud but is not very precise for the arms of the CDT. Indeed, the regions corresponding to the CDT arms display low optical densities (< 0.1) only slightly above the noise level (~ 0.04 , limited by residual fringes on the background). Atom counting in the arms of the CDT is thus more accurate using fluorescence images.

3. Loading and free evaporation in the crossed dipole trap (CDT)

3.1. Dipole trap loading dynamics

We can distinguish two stages in the dynamics of the trap loading. At first, during the MOT/CDT overlap period, atoms are captured mainly in the arms of the CDT without a notable enhancement of the density in the crossing region. In the second phase that follows the extinction of the MOT beams, which we call ‘free evaporation’, the hottest atoms leave the arms and the remaining ones fill the crossing region through thermalization. The quantity of interest is the number of atoms in the central region N_C , which corresponds approximately to the number of atoms with an energy ranging between $-V_{\text{CDT}}^0$ and $-V_{\text{CDT}}^0/2$ (as defined in equation (1)). We show in figure 2 the potential V_{CDT} in the $z = 0$ plane, truncated at three different energy levels. One can see that atoms having energies lower than $V_{\text{CDT}}^0/2$ explore only the central region, as expected. This dense part is the relevant component that matters for further evaporative cooling.

Although both the trapping lasers (CDT and dT) are turned on simultaneously, the CDT is much deeper than the dT, the latter playing a negligible role during this initial stage. In this section, we discuss auxiliary experiments where the dT is absent.

In order to understand the loading dynamics during the first stage, we give a brief overview of the relevant mechanisms (see [11] for a detailed analysis). The loading rate of atoms in the CDT is proportional to the probability of an atom being trapped by the dipole potential and to the atomic flux in the CDT/MOT overlap region. The first term corresponds to the damping of the velocity of an atom when it crosses one arm of the CDT, leading to a reduction in its total energy below the CDT potential depth. The second term is proportional to the spatial density and the average velocity of the atoms in the MOT and thus depends on the temperature of the atoms. The relevant parameters for optimizing the loading rate, namely the atomic density and the temperature, can be adjusted by the ‘dark MOT’ and ‘cold MOT’ phases (see section 2.1). The presence of the dipole potential changes locally the cooling properties, due to the light shifts induced by the CDT laser beams. During this phase, atom accumulation in the trap crossing region is limited by light-assisted inelastic collisions, such as radiative escape.

In the second stage, after the MOT light is extinguished, the trapped atoms thermalize and the sample cools down by evaporative cooling (at a fixed potential depth). Atoms concentrate in the crossing region and the phase-space density shows a substantial increase as compared with the MOT [4].

We have experimentally tested CDT configurations with different beam sizes w_{CDT} (from 30 to 50 μm). A larger beam size helps to trap more atoms during the capture stage due to a higher overlap volume. However, at a given available power, larger beams imply a weakening of the trap stiffness, which in turn penalizes the thermalization after capture. The data presented in this paper were taken with a beam waist of $w_{\text{CDT}} \approx 42 \mu\text{m}$. We obtain very similar results in the case of $w_{\text{CDT}} \approx 35 \mu\text{m}$, but with different optimal powers at each stage. In the next subsection, we will concentrate on the optimization of the laser power to find the optimal trap depth for filling the central region.

3.2. Optimization of CDT loading

In order to characterize the filling dynamics of the crossing region, we define the filling factor $\alpha = N_{\text{C}}/N$ as the fraction of atoms in this region relative to the total number of atoms in the dipole trap. Images such as that in figure 1(b) are processed with a multi-component fitting routine that extracts the temperature, the density, the total atom number N and the number of atoms N_{C} . Details of the fitting procedure are presented in appendix A. The results of the optimization of the CDT power are presented in figure 3, where we plot the evolution of the atom number N_{C} and the filling factor α with time. We fit the function $\alpha(t) = a(1 - e^{-t/\tau}) + b$ to our data.

We look first at a situation in which ‘free evaporation’ occurs at constant CDT power, keeping the same power during the free evaporation phase as during the capture stage. We report in figure 3 the evolution of N_{C} and α with time for three different powers ($P_{\text{CDT}} = 7.9, 13.7$ and 36 W). The values of the loading time τ and the asymptotic value $\alpha_{\infty} = a + b$ of the filling factor obtained from the fit are shown in figure 4. We find an optimal power $P_{\text{CDT}} = 13.7$ W that maximizes both the number of atoms N_{C} and the stationary filling fraction α_{∞} .

In a second set of experiments, the CDT is kept at constant $P_{\text{CDT}} = 13.7$ W during the ‘cold MOT’ phase, and ramped up in 50 ms to another value just after switching off the resonant lasers. As shown in figure 4, ramping up the power to the maximum available power results in quicker loading of the central region ($\simeq 2$ s) and a better filling ratio ($\alpha_{\infty} \simeq 0.6$), the best values being

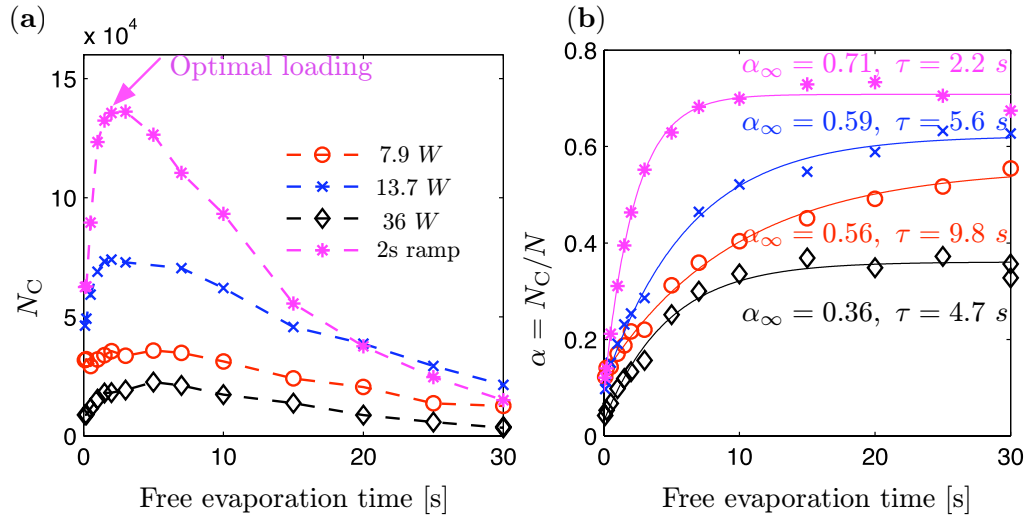


Figure 3. Evolution of the atom number in the center of the CDT (a) and the loading ratio $\alpha = N_C/N$ (b) in four different loading situations: low power (circles), highest power (diamonds), $\sim 1/3$ of maximum power (crosses) and ramping up in 2 s after loading at low power (stars). The loading ratio $\alpha(t)$ is fitted with the function $a(1 - e^{-t/\tau}) + b$. The results of the fit τ and $\alpha_\infty = a + b$ are indicated in (b).

apparently limited by the available laser power. A slower, linear power ramp to $P_{\text{CDT}} = 36$ W in 2 s (also shown in figure 3) leads to a slightly better loading ratio ($\alpha_\infty \simeq 0.7$) and a slightly lower temperature, which altogether results in a higher number of atoms (about twice as many atoms in the center of the CDT, as compared with the loading at constant $P_{\text{CDT}} = 13.7$ W). This particular ramp provides the best starting point we could achieve for the evaporative cooling stage.

The results of the two series of experiments show the existence of an optimal power $P_{\text{CDT}}^{\text{opt}} = 13.7$ W for the loading of the atoms during the period in which the MOT and CDT are simultaneously present. We interpret this observation in the following way. The CDT laser exerts different light shifts on the various hyperfine states in the ground ($3s$) and excited ($3p$) manifolds. These differential light shifts can perturb the laser cooling dynamics in the CDT region and thus degrade the capture efficiency. For instance, if we take the $|g\rangle = |F = 2, m_F = 2\rangle \rightarrow |e_3\rangle = |F' = 3, m_F = 3\rangle$ transition and a π -polarized CDT laser, we find that near the trap bottom, the laser detuning changes according to

$$\delta_{33} = \omega_L - \omega_{33} + \alpha_{33}I, \quad (3)$$

with ω_L being the cooling laser frequency, ω_{33} the ‘bare’ transition frequency and $I = 2P_{\text{CDT}}/\pi w_{\text{CDT}}^2$ the intensity of the CDT laser⁴. For sodium, we find that $\alpha_{33}/2\pi \approx 27$ Hz cm² W⁻¹. For our optimal cooling beam detuning $\delta_{\text{cool}} = \omega_L - \omega_{33} \approx -3.8\Gamma$

⁴ For the calculation we use the data from the NIST atomic spectra database [23] and consider the $3s \rightarrow 3p$, $3p \rightarrow 3d$, $4d$ transitions (see also [24]).

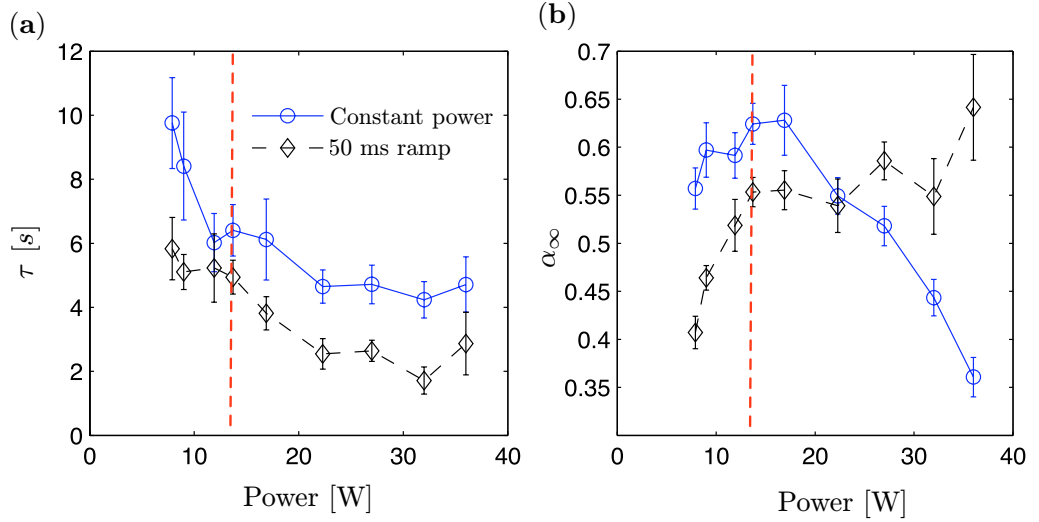


Figure 4. (a) Filling time τ and (b) center filling fraction α_∞ for CDT in two different situations: the solid curve shows the results of the experiments where the CDT laser is held at any time at the same power. The dashed curve denotes the compression experiments where the power starts at $P_{\text{CDT}} = 13.7$ W in the ‘cold MOT’ phase and is ramped up in 50 ms to the final value indicated after switching off the molasses beams. The error bars correspond to 90% confidence bounds on the fit coefficients τ and α_∞ . For $P_{\text{CDT}} = 13.7$ W, both curves should intersect as the experimental sequence is the same. The observed difference indicates systematic variations between different experimental runs, probably due to dipole trap pointing fluctuations and total atom number variations. The vertical dashed line corresponds to the optimal power $P_{\text{CDT}} = 13.7$ W for the ‘cold MOT’ phase.

(see section 2.1), we find that the detuning on the cooling transition vanishes when $I \approx |\delta_{\text{cool}}|/\alpha_{33} \approx 1.4 \times 10^6 \text{ W cm}^{-2}$. Experimentally, the optimum $P_{\text{CDT}}^{\text{opt}} = 13.7$ W corresponds to $I^{\text{opt}} = 4.7 \times 10^5 \text{ W cm}^{-2}$, close to the value calculated above, and a change of detuning from -3.8Γ to $\delta_{33} \approx -2.5\Gamma$. We reached a very similar optimum in another set of experiments with $w'_{\text{CDT}} = 35 \mu\text{m}$, where we found an optimum power $P_{\text{CDT}}^{\text{opt}} = 10$ W corresponding to $I^{\text{opt}} = 5.2 \times 10^5 \text{ W cm}^{-2}$ and a comparable final detuning $\delta_{33} \approx -2.4\Gamma$.

One could think that tuning the cooling beam frequency further than -3.8Γ on the red side of the $|g\rangle \rightarrow |e_3\rangle$ transition could help to mitigate the effect, thus increasing the optimal power and ultimately the number of atoms captured. However, two separate effects work against this strategy. Firstly, this compensation is efficient only near the trap bottom and not across the whole trapping region. Secondly, it brings the MOT beams closer to resonance with neighboring transitions that can shift in opposite ways. For example, the $|g\rangle = |F = 2, m_F = 2\rangle \rightarrow |e_2\rangle = |F' = 2, m_F = 2\rangle$ transition has an intensity dependence $\delta_{22} = \omega_L - \omega_{22} - \alpha_{22}I$, with ω_{22} being the corresponding frequency and $\alpha_{22}/2\pi \approx 16 \text{ Hz cm}^2 \text{ W}^{-1}$. The latter effect is limiting for ^{23}Na , which has a hyperfine structure splitting $\omega_{33} - \omega_{22}$ much smaller than heavier alkalis (^{87}Rb and ^{133}Cs).

4. Two-stage evaporation

4.1. Evaporation in the CDT alone

As pointed out in the introduction, lowering the laser intensity to reduce the trap depth for evaporation is inevitably accompanied by a reduction in trap stiffness (near the trap bottom, the trap frequency ω is proportional to $\sqrt{P/w}$), unlike in magnetic traps, where the depth and confinement are independent. The resulting decrease in density and collision rate can make the cooling due to evaporation stop at low laser power, and this is precisely what is observed in our experiment. For a harmonic trap, the classical phase-space density is given by $\mathcal{D} = N(\hbar\bar{\omega}/k_B T)^3$, where $\bar{\omega}$ stands for the mean trapping frequency. In a simple model where the evaporation parameter $\eta = V_0^{\text{CDT}}/k_B T$ is assumed to be constant and where losses are neglected, the gain in phase-space density when the trap depth is lowered from V_0^{CDT} to V_0^{CDT}/r ($r > 1$ is the reduction factor) is given by [25]

$$\mathcal{D} = \mathcal{D}_0 r^\beta, \quad \beta = \frac{3\eta^2 - 7\eta + 11}{2\eta^2 - 6\eta + 7}. \quad (4)$$

The starting point in our experiment (about 3×10^5 atoms at $T \simeq 100 \mu\text{K}$) corresponds to $\eta \approx 10$ and a phase-space density $\mathcal{D}_0 \sim 10^{-4}$. According to equation (4), evaporating with a reduction factor $r = 200$ leads to a final phase-space density of ~ 0.2 . In our experiment, the laser power is ramped down during evaporation according to

$$V_{\text{CDT}}(t) = V_{\text{CDT}}^0 (1 + t/\tau_{\text{evap}})^{-\alpha_{\text{evap}}}, \quad (5)$$

where the parameters $\tau_{\text{evap}} = 30 \text{ ms}$ and $\alpha_{\text{evap}} = 1.2$ were optimized empirically. Even after optimization we have not been able to achieve a final phase-space density greater than $\sim 10^{-2}$ in the CDT alone⁵. We also observe that the collision rate after $\sim 1 \text{ s}$ is lower than that after 10 s^{-1} and that evaporative cooling stops near this point. Such a collision rate is too low to maintain efficient thermalization and sustain the cooling process.

4.2. Evaporation in the dimple trap

The decrease in evaporation efficiency mentioned in the previous subsection is caused by the relation between trap depth and confinement strength inherent in optical traps. To circumvent the decrease in evaporation efficiency mentioned in the previous subsection, one needs independent control of the trap depth and of the confinement strength. To achieve this aim, we have added a tight ‘dimple’ to the initial trap [8, 20, 26, 27]. We turn on the auxiliary dT together with the main CDT, but keep it at the constant power $P_{\text{dT}} = 200 \text{ mW}$ during the CDT ramp⁶. With the ‘dimple’ addition, the atoms feel a more and more confining potential as they cool, in stark contrast to the situation in the CDT alone. In our experiment, we take advantage of the dissipative nature of evaporative cooling to fill such a dT. As the atoms in the CDT are evaporatively cooled, they get progressively trapped in the stiffer potential, which results in a substantial increase in spatial density [8, 18]. Since the temperature remains the same, this translates into a huge boost in the phase-space density. This is markedly different from an

⁵ The measured phase-space density is lower than the prediction of equation (4). This should be attributed to the crudeness of the model underlying this equation. In particular, three-body losses, which are important at the densities present in the CDT, are not accounted for.

⁶ Keeping the dT power high causes no modification for the CDT loading and compression.

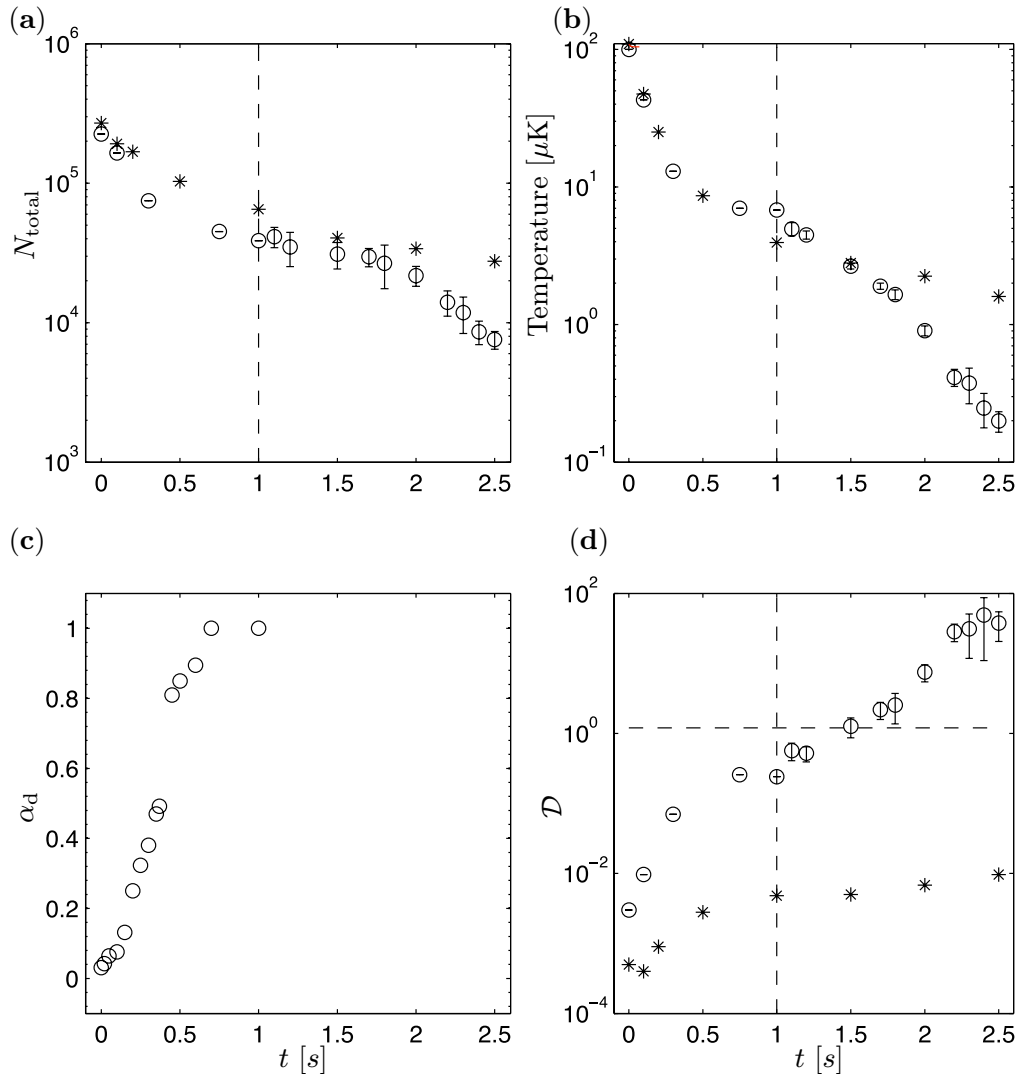


Figure 5. Evaporative cooling trajectories in the combined trap (CDT and dT) (circles) and in the CDT alone (stars). We show the time evolution of the atom number N (a), temperature T (b), dimple filling α_d (c) and phase-space density \mathcal{D} (d).

adiabatic trap compression which increases spatial density but leaves the phase-space density unchanged [28]. After 1 s evaporation in the CDT, the dT power is reduced to provide the final stage of evaporative cooling (see figure 1(c)).

The plots in figure 5 summarize the evaporation dynamics. We show the atom number N , temperature T , dT filling $\alpha_d = N_d/N$, where N_d is the number of atoms present in the dT, and phase-space density \mathcal{D} during the ramp, compared with the evaporation without dT⁷.

⁷ The measurement of α_d is made in the following way: the dT laser is switched off 2.8 ms after the CDT laser, and we let the cloud expand during time-of-flight $t_{\text{ToF}} = 0.2$ ms before taking an absorption image. At this time, atoms released from the CDT have expanded in the x - y plane more than those released from the dT, which is appropriate for counting each component.

From figure 5(c), we observe that almost all atoms accumulate rapidly (within a few hundred of ms) in the dT. At this stage, the atoms are essentially trapped by the dT in the x - y plane and by the weaker CDT in the z -direction. We therefore call this stage ‘evaporative filling’. At the end of it, we obtain a cold sodium gas with high phase-space density and collision rate ($\gamma_{\text{coll}} \approx 2 \times 10^3 \text{ s}^{-1}$), well suited to start a second evaporative cooling stage.

The difference in trapping frequency between the cases with and without dT leads to an increase of about 100 in phase-space density at $t = 1 \text{ s}$. We quantify the evaporation efficiency κ_{evap} from the starting point (N_0, \mathcal{D}_0) to (N_1, \mathcal{D}_1) , using the definition given in [13]:

$$\kappa_{\text{evap}} = - \frac{\ln(\mathcal{D}_1/\mathcal{D}_0)}{\ln(N_1/N_0)}. \quad (6)$$

Typical values in magnetic traps are $\kappa_{\text{evap}} \sim 1$ – 2 . In our experiment, we obtain much better evaporation efficiencies with the use of the dT ($\kappa_{\text{evap}}^{\text{dT}} \simeq 3.5$) than without ($\kappa_{\text{evap}}^{\text{CDT}} \simeq 1.6$).⁸

We pursue the evaporation by reducing the dT depth, with an exponential ramp from $P_{\text{dT}} = 200$ to 2 mW in 1.5 s , with a time constant $\tau_{\text{dT}} = 0.6 \text{ s}$. This results in a phase-space density increase and a crossing of the BEC threshold after $\sim 1 \text{ s}$ ramping, with $\simeq 2 \times 10^4$ atoms at $T \simeq 1 \mu\text{K}$. At the end of this ramp, we obtain an almost pure BEC with $\simeq 10^4$ atoms.

Finally, we note that the dT is used here in quite a different way compared to the experiment reported in [26, 27]. In these works, the authors studied an adiabatic process, in which the gain in phase-space density is obtained isentropically by modifying the trap potential shape [29]. In the present work, the entropy is reduced by evaporative cooling as the transfer between the CDT and the dT proceeds.

5. Conclusion and prospects

We have demonstrated a method to achieve Bose–Einstein condensation of ^{23}Na in an all-optical experimental setup. We have shown the importance of adapting the trapping potential to the MOT cooling dynamics for optimizing the capture in the arms of the crossed trap. In the free evaporation step that follows, an increase in trap depth leads to a fast transfer of atoms from the arms to the central region, providing thus a dense sample. We have also described the implementation of a two-step evaporation stage using a tightly focused ‘dT’. ‘Evaporative filling’ of the dT occurs at almost the same atom number and temperature as in the CDT alone. As a result, the phase-space density increases as $(\bar{\omega}_{\text{dT}}/\bar{\omega}_{\text{CDT}})^3$, where $\bar{\omega}_{\text{dT}}$ is the dT average frequency and $\bar{\omega}_{\text{CDT}}$ the CDT average frequency at low power. Experimentally this corresponds to a large gain in phase-space density, of ~ 100 . After a final evaporation stage in the dT, we are able to obtain almost pure BECs containing $\sim 10^4$ atoms.

The efficient ‘evaporative filling’ of the dT suggests to generalize the scheme by adding a second, even smaller dT to shorten the time to reach Bose–Einstein condensation. Such a scheme with imbricated evaporative cooling steps (like the layers of an ‘atomic matryoshka’) can be taken into consideration if the aim is the production of BECs with small atom number, confined in a microscopic potential [30–32].

⁸ We have found experimentally that turning on the dT at a later stage during the evaporation ramp still results in a boost in phase-space density. However, the cooling is not as efficient, so that the final phase-space density and the evaporation efficiency are both slightly worse.

Acknowledgments

We thank Lingxuan Shao and Wilbert Kruithof for assistance with experiments. DJ acknowledges financial support from DGA (contract no. 2008/450). LDS acknowledges financial support from the EU IEF (grant no. 236240). This work was supported by IFRAF, the EU (MIDAS STREP project) and DARPA (OLE project). Laboratoire Kastler Brossel is a Unité Mixte de Recherche (UMR no. 8552) of CNRS, ENS and UPMC.

Appendix A. Analysis of CDT images

A figure of merit for the loading in the CDT is the number of atoms in the crossing region of the trap, as mainly these atoms will participate in evaporative cooling. We will take the ratio between the atoms in this region and the atoms in the arms as an indicator of the loading efficiency. We fit the atomic density profiles with a sum of three Gaussians, two of them fitting the arms region and the last one fitting the central region,

$$f_{2D}(x, y) = \sum_{j=1}^3 G(A_j; x_j, y_j; \sigma_{jx}, \sigma_{jy}), \quad (\text{A.1})$$

with $G(A, x, y, \sigma_x, \sigma_y) = Ae^{-1/2(x/\sigma_x)^2 - 1/2(y/\sigma_y)^2}$. Here A is the amplitude and σ_x and σ_y are the sizes of the distribution along the directions x and y . The first two components 1, 2 model the arms so that $\sigma_{1y} \gg \sigma_{1x}$ and $\sigma_{2y} \gg \sigma_{2x}$. The third component models the denser crossing region. The second arm propagates with an angle θ : $(x_2, y_2) = (x_1 \cos(\theta) + y_1 \sin(\theta), -x_1 \sin(\theta) + y_1 \cos(\theta))$. Each arm is supposed to be radially symmetric; the size in the z -direction is therefore taken as equal to the radial size in the (x, y) plane. From the sizes and the calibration of the total fluorescence counts on the CCD with the atom number measured from an absorption image, we infer the atom number in each of the components N_1 , N_2 and N_3 .

In order to evaluate how well equation (A.1) can fit the density profile, we perform the fit on a computed density profile of an atomic cloud at thermal equilibrium in a CDT potential $U(\mathbf{r}) = V_{\text{CDT}}(\mathbf{r})$ (see equation (1)), for $P_{\text{CDT}} = 13.7 \text{ W}$ and $w_{\text{CDT}} = 42 \mu\text{m}$. For a classical gas, the phase-space density $f(\mathbf{r}, \mathbf{p})$ is given by

$$f(\mathbf{r}, \mathbf{p}) = \frac{1}{Z} e^{-[p^2/2M + U(\mathbf{r})]/k_B T} \Theta(-p^2/2M - U(\mathbf{r})) \quad (\text{A.2})$$

with Z being the partition function chosen such that $\int f(\mathbf{r}, \mathbf{p}) \frac{d^3 r d^3 p}{(2\pi\hbar)^3} = 1$, and Θ the Heaviside step function. An integration of $f(\mathbf{r}, \mathbf{p})$ along the imaging direction z yields a two-dimensional (2D) profile $n_{2D}^{\text{sim}}(x, y)$,

$$n_{2D}^{\text{sim}}(x, y) = \int dz \int f(\mathbf{r}, \mathbf{p}) \frac{d^3 \mathbf{p}}{(2\pi\hbar)^3} = \int dz e^{-U(\mathbf{r})/k_B T} \Gamma_{\text{inc}} \left(\frac{U(\mathbf{r})}{k_B T}, \frac{3}{2} \right), \quad (\text{A.3})$$

where Γ_{inc} is the incomplete gamma function. We also calculate the density of states $\rho(\epsilon)$ (with $-V_{\text{CDT}}^0 < \epsilon < 0$),

$$\rho(\epsilon) = \int \frac{d^3 \mathbf{r} d^3 \mathbf{p}}{(2\pi\hbar)^3} \delta(\epsilon - p^2/2M - U(\mathbf{r})) = \frac{1}{(2\pi)^2} \left(\frac{2m}{\hbar^2} \right)^{3/2} \int d\mathbf{r} \sqrt{\epsilon - U(\mathbf{r})}. \quad (\text{A.4})$$

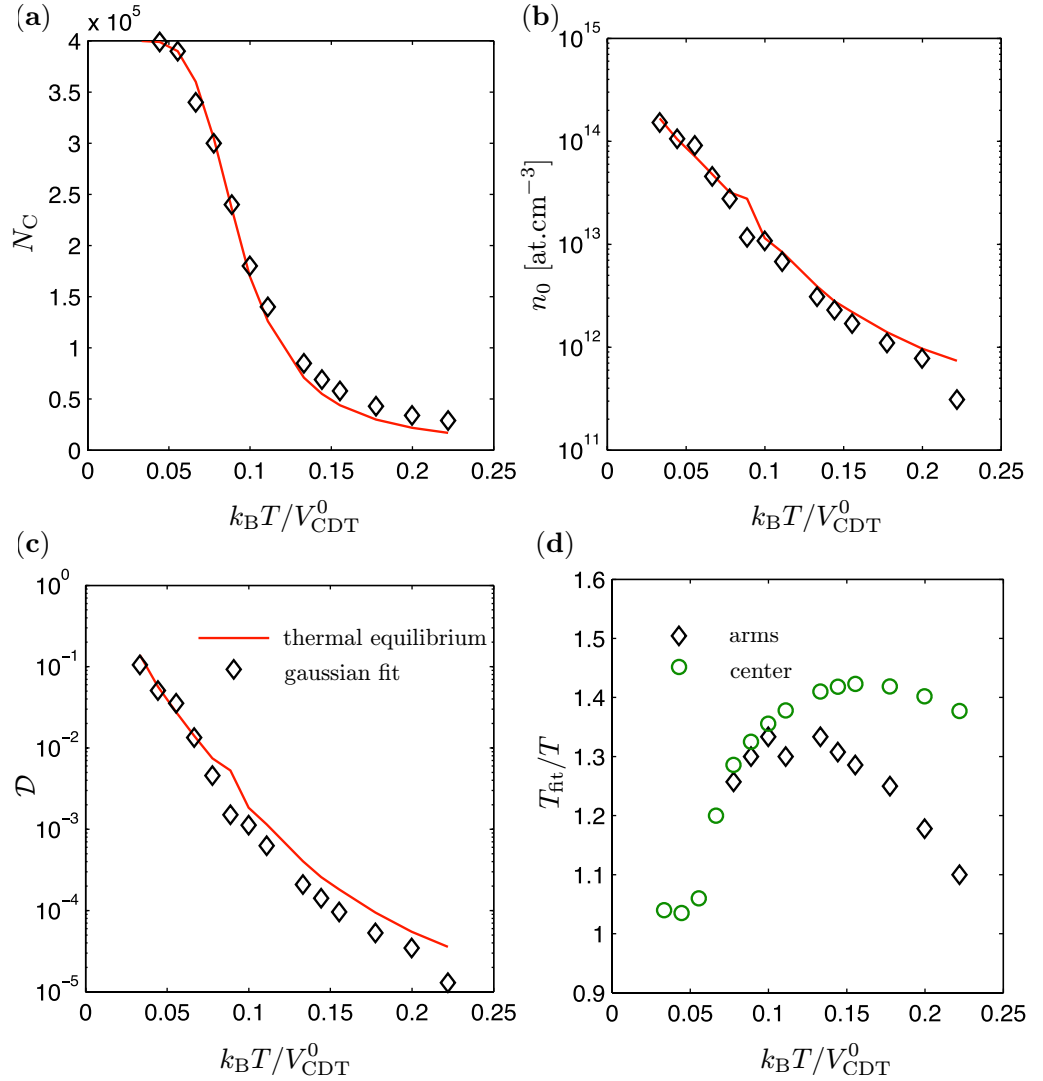


Figure A.1. Test of the multicomponent fitting routine used to analyze CDT images. For (a), (b) and (c), black diamonds show the result from the fit. In (a), the center atom number is calculated from the density of states and shown as a solid line. For the solid lines in (b) and (c), n_0 and \mathcal{D} are taken from the formulae at thermal equilibrium. In (d), the temperatures extracted from the size of the arms and the size of the central component are compared with the ones used to compute the distribution.

This can be used to determine the number of atoms N_C that have an energy between $-V_{\text{CDT}}^0$ and $-V_{\text{CDT}}^0/2$,

$$N_C = N(-V_{\text{CDT}}^0 \leq \epsilon \leq -V_{\text{CDT}}^0/2) = n_0 \Lambda_{\text{dB}}^3 \int_0^{V_{\text{CDT}}^0/2} d\epsilon \rho(\epsilon) e^{-\epsilon/k_B T}, \quad (\text{A.5})$$

with n_0 being the density in the center of the trap, and $\Lambda_{\text{dB}} = h/\sqrt{2\pi m k_B T}$ the thermal de Broglie wavelength. We take N_C as an estimate of the number of atoms in the central region. Equations (A.4) and (A.5) are evaluated numerically using Monte-Carlo integration.

We apply to the simulated profiles n_{2D}^{sim} the same fitting routine as that used for the experimental images. In figure A.1, we compare the fit output with the parameters used in the simulation.

As one can see, the number of atoms in the center is found to be very close to N_C . This validates our method to estimate the loading ratio $\alpha = N_C/N_{\text{tot}}$ with the result from the fit $N_3/(N_1 + N_2 + N_3)$. Note, however, that the procedure systematically overestimates the temperature in the arms by $\sim 30\%$. This is due to the Gaussian shape of the trap that leads to a radial density profile that is wider than the profile created by a harmonic trap with the same curvature. We checked that, for a truncated harmonic trap, the fitted temperature is equal to the temperature T obtained for the simulated profile (equation (A.3)).

References

- [1] Bloch I, Dalibard J and Zwerger W 2008 Many-body physics with ultracold gases *Rev. Mod. Phys.* **80** 885–964
- [2] Bouyer P and Kasevich M A 1997 Heisenberg-limited spectroscopy with degenerate Bose–Einstein gases *Phys. Rev. A* **56** R1083–R1086
- [3] Gross C, Zibold T, Nicklas E, Estève J and Oberthaler M K 2010 Nonlinear atom interferometer surpasses classical precision limit. *Nature* **464** 1165–9
- [4] Barrett M D, Sauer J A and Chapman M S 2001 All-optical formation of an atomic Bose–Einstein condensate *Phys. Rev. Lett.* **87** 010404
- [5] Kinoshita T, Wenger T and Weiss D S 2005 All-optical Bose–Einstein condensation using a compressible crossed dipole trap *Phys. Rev. A* **71** 011602
- [6] Cennini G, Ritt G, Geckeler C and Weitz M 2003 Bose–Einstein condensation in a CO₂-laser optical dipole trap *Appl. Phys. B: Lasers Opt.* **77** 773–9
- [7] Granade S R, Gehm M E, O’Hara K M and Thomas J E 2002 All-optical production of a degenerate Fermi gas *Phys. Rev. Lett.* **88** 120405
- [8] Weber T, Herbig J, Mark M, Nägerl H-C and Grimm R 2003 Bose–Einstein condensation of cesium *Science* **299** 232–5
- [9] Dumke R, Johanning M, Gomez E, Weinstein J D, Jones K M and Lett P D 2006 All-optical generation and photoassociative probing of sodium Bose–Einstein condensates *New J. Phys.* **8** 64
- [10] Stenger J, Inouye S, Stamper-Kurn D M, Miesner H J, Chikkatur A P and Ketterle W 1998 Spin domains in ground-state Bose–Einstein condensates *Nature* **396** 345–8
- [11] Kuppens S J M, Corwin K L, Miller K W, Chupp T E and Wieman C E 2000 Loading an optical dipole trap *Phys. Rev. A* **62** 013406
- [12] Adams C S, Lee H J, Davidson N, Kasevich M and Chu S 1995 Evaporative cooling in a crossed dipole trap *Phys. Rev. Lett.* **74** 3577–80
- [13] Ketterle W, Van Druten N J, Bederson B and Walther H 1996 *Evaporative Cooling of Trapped Atoms* vol 37 (New York: Academic) pp 181–236
- [14] Hung C-L, Zhang X, Gemelke N and Chin C 2008 Accelerating evaporative cooling of atoms into Bose–Einstein condensation in optical traps *Phys. Rev. A* **78** 011604
- [15] Clément J F, Brantut J P, Robert-de Saint-Vincent M, Nyman R A, Aspect A, Bourdel T and Bouyer P 2009 All-optical runaway evaporation to Bose–Einstein condensation *Phys. Rev. A* **79** 061406
- [16] Lin Y J, Perry A R, Compton R L, Spielman I B and Porto J V 2009 Rapid production of ⁸⁷Rb Bose–Einstein condensates in a combined magnetic and optical potential *Phys. Rev. A* **79** 063631
- [17] Ma Z-Y, Thomas A M, Foot C J and Cornish S L 2003 The evaporative cooling of a gas of caesium atoms in the hydrodynamic regime *J. Phys. B: At. Mol. Opt. Phys.* **36** 3533
- [18] Ma Z-Y, Foot C J and Cornish S L 2004 Optimized evaporative cooling using a dimple potential: an efficient route to Bose–Einstein condensation *J. Phys. B: At. Mol. Opt. Phys.* **37** 3187

- [19] Comparat D, Fioretti A, Stern G, Dimova E, Laburthe B Tolra and Pillet P 2006 Optimized production of large Bose–Einstein condensates *Phys. Rev. A* **73** 043410
- [20] Mimoun E, De Sarlo L, Jacob D, Dalibard J and Gerbier F 2010 Fast production of ultracold sodium gases using light-induced desorption and optical trapping *Phys. Rev. A* **81** 8
- [21] Ketterle W, Davis K B, Joffe M A, Martin A and Pritchard D E 1993 High densities of cold atoms in a dark spontaneous-force optical trap *Phys. Rev. Lett.* **70** 2253–6
- [22] Kaiser R, Westbrook C, David F, Stamper-Kurn D and Ketterle W 2001 *Spinor Condensates and Light Scattering from Bose–Einstein Condensates* vol 72 (Berlin: Springer) pp 139–217
- [23] Ralchenko Yu, Kramida A E, Reader J and the NIST ASD Team 2010 *NIST Atomic Spectra Database (Version 4.0)*
- [24] Viering K 2006 Spatially resolved single atom detection of neutral atoms *Master's Thesis* University of Texas, Austin
- [25] O'Hara K M, Gehm M E, Granade S R and Thomas J E 2001 Scaling laws for evaporative cooling in time-dependent optical traps *Phys. Rev. A* **64** 051403(R)
- [26] Stamper-Kurn D M, Miesner H J, Chikkatur A P, Inouye S, Stenger J and Ketterle W 1998 Reversible formation of a Bose–Einstein condensate *Phys. Rev. Lett.* **81** 2194–7
- [27] Garrett M C, Ratnapala A, van Ooijen E D, Vale C J, Weegink K, Schnelle S K, Vainio O, Heckenberg N R, Rubinsztein-Dunlop H and Davis M J 2011 Growth dynamics of a Bose–Einstein condensate in a dimple trap without cooling *Phys. Rev. A* **83** 013630
- [28] Ketterle W and Pritchard D E 1992 Atom cooling by time-dependent potentials *Phys. Rev. A* **46** 4051–4
- [29] Pinkse P W H, Mosk A, Weidemüller M, Reynolds M W, Hijmans T W and Walraven J T M 1997 Adiabatically changing the phase-space density of a trapped Bose gas *Phys. Rev. Lett.* **78** 990–3
- [30] Kolomeisky E B, Straley J P and Kalas R M 2004 Ground-state properties of artificial bosonic atoms, Bose interaction blockade, and the single-atom pipette *Phys. Rev. A* **69** 063401
- [31] Chuu C S, Schreck F, Meyrath T P, Hanssen J L, Price G N and Raizen M G 2005 Direct observation of sub-Poissonian number statistics in a degenerate Bose gas *Phys. Rev. Lett.* **95** 260403
- [32] Dudarev A M, Raizen M G and Niu Q 2007 Quantum many-body culling: production of a definite number of ground-state atoms in a Bose–Einstein condensate *Phys. Rev. Lett.* **98** 063001